(Received 14 June 2026, Accepted 19 July 2026, Scheduled 3 August 2026)

Broadband SIW Slot Antenna Based on Split Magnetic-Electric Dipole Multi-Mode Coupling

Mingming Gao[1,2], Bowen Tao[1,2,*], Ruize Huang[2], Xuan Du[2], and Shibo Sun[2]

[1]Ordos Institute of Liaoning Technical University, Ordos 017000, China
[2]School of Electronic and Information Engineering, Liaoning Technical University, Huludao 125105, China

ABSTRACT: To realize a compact and low-profile Ka-band SIW antenna with continuous wideband operation, a wideband SIW slot antenna based on split magnetic-electric dipole multi-mode coupling is proposed. The central design idea is to transfer electromagnetic energy from the lower SIW cavity to the upper radiating layer through aperture coupling and to merge two adjacent resonant modes generated by the electric- and magnetic-dipole components. The antenna employs a dual-layer configuration. The lower layer consists of an SIW feeding cavity and a coupling slot, and the upper layer incorporates split arc-shaped patches, a central coupling patch, metallized vias, and a cross-shaped perturbation structure. The split patches mainly generate the high-frequency electric-dipole mode, while the central coupling patch and metallized vias introduce an adjacent lower-frequency magnetic-dipole mode. The cross-shaped perturbation structure further optimizes the impedance transition between the two modes. The simulated results show that the antenna achieves an impedance bandwidth of 26.35–29.20 GHz for $|S_{11}| < -10$ dB and a peak realized gain of approximately 8.15 dBi at 28 GHz. The fabricated prototype exhibits a measured impedance bandwidth of approximately 26.8–29.1 GHz. In addition, the simulated multifrequency radiation patterns and efficiency results demonstrate relatively stable broadside radiation characteristics within the operating band. The proposed antenna provides a compact and readily integrated solution for Ka-band millimeter-wave communication systems.

1. INTRODUCTION

With the rapid development of millimeter-wave communication technologies, Ka-band antennas have attracted considerable attention owing to their significant application value in high-speed wireless communications, satellite communications, radar sensing, and 5G mmWave systems [1, 2]. Compared with conventional microwave bands, mmWave bands offer substantially richer spectral resources and higher data throughput. However, the deployment of mmWave systems imposes increasingly stringent requirements on antennas' impedance bandwidth, gain, efficiency, size, and integration density. Consequently, the design of wideband, low-profile, and compact mmWave antennas with stable radiation characteristics is of considerable significance.

Conventional microstrip patch antennas offer advantages of a simple structure, ease of fabrication, and straightforward integration; however, they typically suffer from narrow operating bandwidths and are susceptible to dielectric loss and reduced radiation efficiency at mmWave frequencies. In contrast, the substrate-integrated waveguide (SIW) combines the low loss and excellent shielding characteristics of conventional metallic waveguides with the integration convenience of microstrip circuits and has become one of the most important planar guided-wave structures for mmWave circuits and antennas [3, 4]. By introducing periodic rows of metallized vias on both sides of a dielectric substrate, the SIW forms an equivalent waveguide cavity within a planar circuit, thereby achieving low-loss transmission and favorable electromagnetic shielding performance [5, 20].

However, conventional SIW cavity-backed slot antennas generally exhibit a narrow impedance bandwidth due to the high quality factor of the cavity. Ref. [5] reported a planar SIW cavity-backed slot antenna achieving a fractional bandwidth of only 1.70% at microwave frequencies. To improve the bandwidth, researchers have proposed a variety of enhancement strategies. Ref. [6] simultaneously excited two hybrid modes within the SIW cavity and merged them across the operating band, extending the impedance bandwidth to 6.30%. Ref. [7] introduced a superstrate with a rectangular slot window above the cavity to provide an additional resonance, improving the bandwidth and gain to a fractional bandwidth of approximately 7.07%; however, the superstrate increased both the profile height and fabrication complexity. Ref. [9] employed a triangular slot combined with two different feeding transitions to improve impedance matching; however, the bandwidth enhancement remained limited, with a fractional bandwidth of only 4.36%. Ref. [10] proposed a dual-band multilayer SIW differential slot antenna to achieve dual-band operation by exciting multiple cavity modes; however, its dual-band nature restricts its applicability in continuous wideband scenarios. These studies indicate that the high-quality factor of the SIW cavity imposes a fundamental constraint on wideband operation; this difficulty is further aggravated at mmWave frequencies, where increased dielectric loss, tighter fabrication tolerances, and more sensitive interlayer coupling intensify the challenge of bandwidth enhancement.

* Corresponding author: Bowen Tao (1831955785@qq.com).

Recent studies have continued to investigate SIW cavity-backed slot antennas and magnetic-electric dipole antennas for compact and broadband wireless systems. Ref. [23] reviewed the development and bandwidth-enhancement methods of SIW cavity-backed slot antennas. Ref. [24] proposed a compact dual-slot SIW cavity-backed antenna and established an equivalent cavity model to explain its resonant behavior. For Ka-band applications, Ref. [25] employed a novel slot with a shorting via to excite multiple adjacent cavity modes, thereby achieving broadband operation. Ref. [26] introduced a fragmented dipole arm into a low-profile millimeter-wave magnetic-electric dipole antenna to generate an additional resonance and broaden the impedance bandwidth. More recently, Ref. [27] utilized two closely spaced modes in a hexagonal SIW cavity to enhance the operating bandwidth. These studies demonstrate that multi-mode excitation and the combination of electric- and magnetic-dipole radiation modes are effective approaches for bandwidth enhancement. Nevertheless, compact Ka-band SIW antennas with a simple split magnetic-electric dipole coupling configuration remain worthy of further investigation.

To further broaden bandwidth and improve radiation performance, multilayer stacked structures with interlayer coupled feeding have been explored [14–17, 19]. The underlying principle is to excite multiple adjacent resonant modes through the coordinated coupling among the feeding slot, primary radiating element, and parasitic patches, such that the resonant peaks merge within the target band to achieve bandwidth extension. Among the available radiator topologies, a magnetic-electric dipole structure offers distinct advantages in terms of wideband impedance matching and pattern stability, as it simultaneously exploits the radiation characteristics of both electric and magnetic dipoles [18]. Therefore, integrating SIW slot feeding with a split magnetic-electric (ME) dipole structure provides an effective route for realizing wideband, low-profile Ka-band mmWave antennas.

Based on the above analysis, this study proposes a wideband SIW slot antenna based on a split magnetic-electric dipole with multi-mode coupling. The distinguishing contribution of this work does not lie in the use of SIW feeding or aperture coupling alone, but in the coordinated mode-engineering scheme implemented in a compact dual-layer structure. Specifically, the split arc-shaped patches generate a high-frequency electric-dipole mode; the central coupling patch and metallized vias introduce an adjacent lower-frequency magnetic-dipole mode; and the cross-shaped perturbation structure balances the impedance transition between the two resonances. Consequently, the two resonant modes are merged into a continuous operating band without employing an antenna array, a high-profile superstrate, or a complicated multilayer feeding network. Compared with the array-based SIW magneto-electric dipole antennas reported in [19] and [22], the proposed antenna is implemented as a compact two-layer single element and does not require a corporate feed network or an enlarged array aperture. Compared with the multimode SIW cavity-backed slot antenna in [25], the proposed design introduces a split magneto-electric dipole radiator, in which the split arc-shaped patches, the central coupling patch with metallized vias, and the cross-shaped perturbation structure control the electric-dipole mode, magnetic-dipole mode, and intermodal impedance transition, respectively. The simulated results demonstrate that the proposed antenna satisfies $|S_{11}| \leq -10$ dB over 26.35–29.20 GHz, corresponding to a fractional impedance bandwidth of approximately 10.26%. The fabricated prototype achieves a measured impedance bandwidth of approximately 26.8–29.1 GHz. In addition, the simulated multi-frequency radiation patterns, realized gain, and efficiency results indicate relatively consistent broadside radiation characteristics over the investigated frequency range.

2. ANTENNA DESIGN

2.1. Antenna Configuration

The proposed antenna employs a dual-layer stacked configuration based on Rogers RT/Duroid 5880 dielectric substrates, with a relative permittivity of $\epsilon_r = 2.2$ and a loss tangent of $\tan\delta = 0.0009$. The antenna consists of a bottom SIW feeding layer and a top split magnetic-electric dipole radiating layer, which are interconnected through a coupling slot to achieve interlayer energy coupling, thereby forming a complete "feeding-coupling-radiation" energy transmission chain. Fig. 1 shows a 3D structural diagram of the proposed antenna.

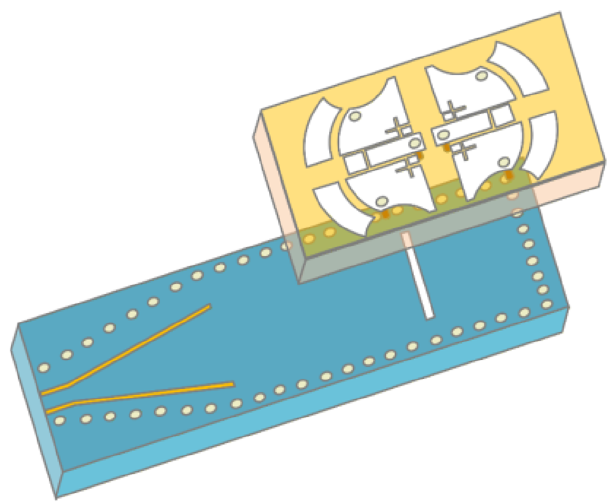

FIGURE 1. Schematic diagram of the SIW slot antenna.

(1) The bottom layer is an SIW feeding cavity, which primarily consists of an input transition structure, two rows of periodic metallized vias, a metal ground plane, and a coupling slot etched on the top metal surface. The two rows of periodic metallized vias act as the sidewalls of a metallic waveguide, effectively confining the electromagnetic energy within the SIW cavity and thereby enabling low-loss transmission. The equivalent width of the SIW can be approximated as:

$$W_{\mathit{eff}} = W_{\mathrm{SIW}} - \frac{d^2}{0.95p} \tag{1}$$

where W_{SIW} is the physical width of the SIW; d is the diameter of the metallized vias; and p is the via pitch. To effectively suppress energy leakage through the gaps between adjacent vias, the via pitch and diameter should satisfy $p < 2d$ [3].

TABLE 1. Geometrical parameters of the proposed antenna.

Parameter	Value (mm)	Parameter	Value (mm)	Parameter	Value (mm)
L	18.3	L_s	4.0	L_{tt}	0.9
h	1.016	W_2	0.3	m_1	0.8
W_{siw}	7.0	P_1	0.8	R	2.6
L_2	10.8	m_2	1.1	R_1	0.9
L_{tra}	6.5	m	1.0	l	4.3
l_2	2.0	d_1	4.0	d_2	1.2

The input transition structure is employed to convert the port excitation into the SIW's dominant-mode propagation and to improve input impedance matching to reduce reflection. The coupling slot etched on the top of the SIW cavity can be modeled as an aperture-type magnetic current source. Without any direct metallic connection, this slot couples the electromagnetic energy stored in the bottom SIW cavity to the upper radiating layer. Therefore, the length, width, and offset of the coupling slot are the key parameters that determine the coupling strength, the resonant frequency, and the impedance bandwidth.

The initial dimensions and position of the coupling slot were determined according to the dominant-mode field distribution in the SIW cavity and subsequently optimized using full-wave simulations. The slot was placed at the transverse symmetry plane of the SIW cavity and directly beneath the central coupling patch. This zero-offset arrangement enables approximately symmetric excitation of the two split radiating sections and reduces possible radiation-pattern asymmetry.

The initial slot length was selected according to the effective half-wavelength around the target frequency of $28\,\mathrm{GHz}$, and a narrow slot width was adopted to prevent excessive interlayer coupling. The slot width was fixed at $W_2 = 0.3\,\mathrm{mm}$ considering both the required coupling strength and fabrication capability. The slot length was then parametrically investigated over 3.8–$4.2\,\mathrm{mm}$. An excessively short slot results in insufficient coupling and increased separation between the two resonances, whereas an excessively long slot produces an overly-coupled response and deteriorates high-frequency matching. The optimized value $L_s = 4.0\,\mathrm{mm}$ provides the most balanced resonant positions and the best in-band impedance matching.

(2) The top radiating structure consists of split arc-shaped patches, a central coupling patch, a cross-shaped perturbation element, and metallized vias, whose coordinated operation constitutes a complete magnetic-electric (ME) dipole radiator. The central coupling patch is positioned directly above the coupling slot; it captures the electromagnetic energy coupled through the slot and redistributes the surface current to the arc-shaped patches on both sides, while also altering the current path in the central region and lengthening the equivalent current trajectory to excite a lower-frequency resonant mode.

The split arc-shaped patches serve as the primary radiating element and are equivalent to a horizontal electric dipole: compared with a conventional rectangular patch, they lengthen the surface current path and introduce strong edge coupling at the split gaps, exciting an electric-dipole-type resonance at higher frequencies while maintaining a compact aperture. The metallized vias connect the upper and lower metal surfaces, providing a vertical conduction path for the surface current and acting as a vertical magnetic dipole to enhance the magnetic-dipole-type radiation response, and the cross-shaped perturbation element finely tunes the local current distribution and equivalent electrical length by introducing a capacitive perturbation, thereby optimizing the impedance transition between the two types of elements.

Through this synergistic operation, the adjacent electric and magnetic resonant modes are coupled and merged within the target band; being spatially orthogonal and complementary in phase, they jointly achieve wideband impedance matching and a stable broadside radiation pattern. The overall dimensions of the antenna proposed in this study are $18.3 \times 7 \times 2.032\,\mathrm{mm}^3$. The specific antenna parameters are listed in Table 1, and Fig. 2 shows the antenna's planar structure.

2.2. Antenna Evolution

To elucidate the mechanism underlying the wideband characteristic of the proposed antenna, Fig. 3 illustrates the evolution of the radiating structure. The three evolutionary stages are denoted as Antenna a, Antenna b, and Antenna c, and their corresponding simulated S_{11} curves are compared in Fig. 4.

Antenna a represents the initial structure, in which only a pair of split arc-shaped patches is placed on the top metal surface as the primary radiating element. This structure is equivalent to a horizontal electric dipole and excites only a single resonant mode at approximately $28.1\,\mathrm{GHz}$. As shown in Fig. 4, its $|S_{11}| \leq -10\,\mathrm{dB}$ impedance bandwidth is confined to 27.69–$28.44\,\mathrm{GHz}$, corresponding to a fractional bandwidth of merely 2.67%. This narrowband resonant response is inadequate for broadband millimeter-wave applications.

For Antenna b, a central coupling patch loaded with two metallized vias is introduced directly above the coupling slot. The central coupling patch enhances the energy coupling between the SIW slot and the upper radiating structure and lengthens the equivalent current path in the central region, introducing an adjacent lower-frequency resonant mode. Meanwhile, the two metallized vias provide a vertical conduction path for the surface current, exciting a magnetic-dipole component. Under the combined effect of the electric and magnetic dipoles, the impedance bandwidth is markedly broadened to 26.34–$29.89\,\mathrm{GHz}$, corresponding to a fractional bandwidth of approximately 12.6%, thereby achieving a crucial transition from narrowband to wideband operation. However, the hump between

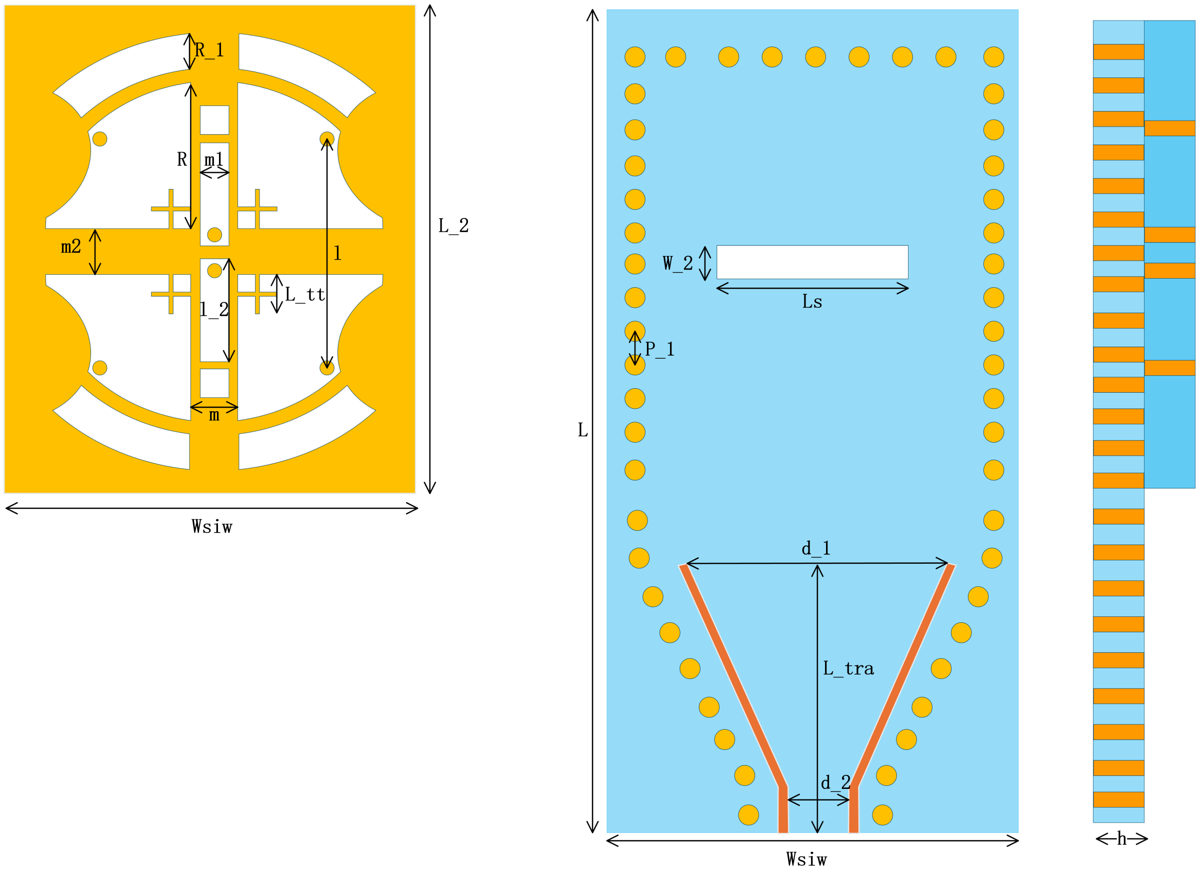

FIGURE 2. Plan view of the SIW slot antenna.

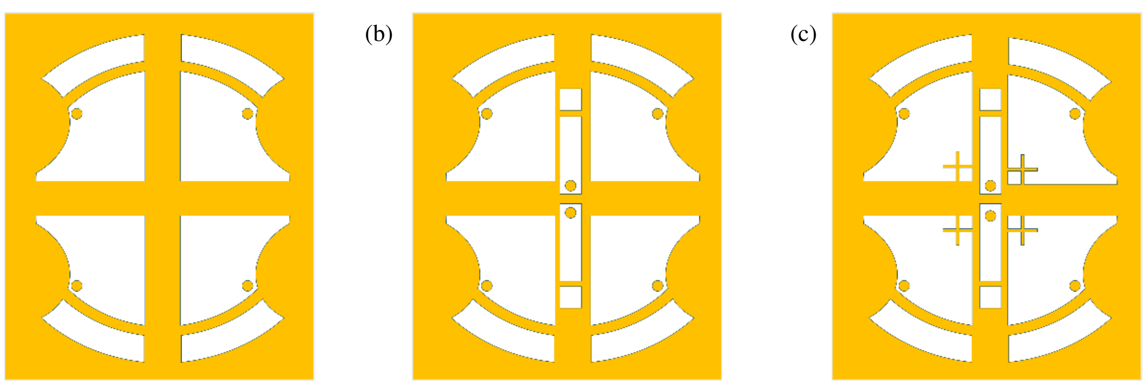

FIGURE 3. Schematic diagram of the evolution of the SIW slot antenna.

the two resonances reaches only about −10.3 dB at this stage, indicating shallow in-band matching with an insufficient margin.

To improve in-band matching, Antenna c incorporates a cross-shaped perturbation structure based on Antenna b to form the final radiating configuration. Embedded between the central coupling patch and the split arc-shaped patches, this structure introduces a capacitive perturbation to redistribute the local current and tune the equivalent electrical length, thereby optimizing the impedance transition between adjacent resonant modes. As shown in Fig. 4, the matching depths of both resonances are notably deepened after its introduction: the lower resonance deepens from approximately −22.7 dB to −25.5 dB and the higher resonance from approximately −19 dB to −27.3 dB, while the central hump is substantially lowered from about −10.3 dB to −18 dB, yielding more sufficient in-band matching and significantly improved flatness. Ultimately, the antenna achieves stable wideband matching with a fractional bandwidth of 10.26% over 26.35–29.20 GHz.

The above evolution demonstrates that the wideband performance of the proposed antenna is realized through the synergistic operation of the split arc-shaped patches, central coupling patch, and cross-shaped perturbation structure: the split arc-shaped patches provide the fundamental electric-dipole mode;

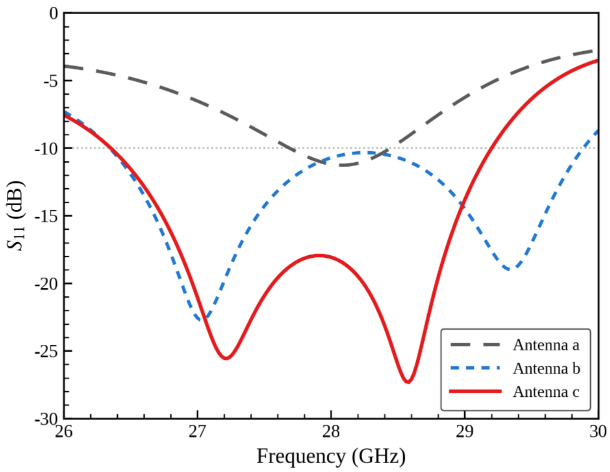

FIGURE 4. Simulated reflection coefficients of the antenna evolution structures.

the central coupling patch and vias introduce a magnetic-dipole component and substantially broaden the bandwidth; and the cross-shaped perturbation structure further deepens the resonance matching and suppresses the in-band hump, enabling the antenna to achieve sufficient and stable impedance matching while maintaining its wideband characteristic.

2.3. Operating Mechanism Analysis

To provide a deeper insight into the wideband radiation mechanism of the proposed antenna, the surface current and electric-field distributions of the radiating structure at the two resonant frequencies are presented in Figs. 5 and 6, respectively.

At the higher resonant frequency of 28.58 GHz, as shown in Fig. 5(a), the surface current becomes highly concentrated on the central coupling patch and cross-shaped perturbation structure, forming a strong horizontal current path that is equivalent to a horizontal electric dipole. Correspondingly, as shown in Fig. 6(a), the electric field spreads from the center toward the surrounding split arc-shaped patches, exhibiting typical electric-dipole radiation characteristics. Therefore, the antenna operates in an electric-dipole-dominated mode at this frequency.

At the lower resonant frequency of 27.3 GHz, as shown in Fig. 5(b), the surface current is mainly distributed along the split arc-shaped patches on both sides, following a relatively long path around the arc edges. Meanwhile, as observed in Fig. 6(b), the electric field is highly concentrated around the central coupling patch and the cross-shaped perturbation structure, forming a strong equivalent magnetic current in this region. At this frequency, a pronounced vertical current component is excited along the metallized vias, which, together with the horizontal surface current, constitutes an equivalent magnetic dipole. Consequently, the antenna operates in a magnetic-dipole-dominated mode at this frequency.

A comparison of the two resonant frequencies reveals that the strong regions of the electric field and surface current are complementarily distributed between the lower and higher bands: at the lower frequency, the electric field concentrates at the center, whereas the current is distributed at the periphery; at the higher frequency, the current concentrates at the center, whereas the electric field extends to the periphery. This spatially orthogonal and phase-complementary behavior of the electric and magnetic dipoles is the characteristic signature of magnetic-electric dipole radiation. The two resonant modes were coupled and merged within the target band, enabling the antenna to broaden its impedance bandwidth while maintaining a stable broadside radiation pattern and good pattern consistency.

The multi-mode coupling mechanism can also be quantitatively verified from the antenna-evolution results. Antenna a, which contains only the split arc-shaped patches, produces a single electric-dipole-type resonance around 28.1 GHz and achieves a fractional impedance bandwidth of only 2.67%. After the central coupling patch and metallized vias are introduced in Antenna b, an additional lower-frequency magnetic-dipole-type resonance is generated, and the fractional bandwidth is increased to approximately 12.6%. However, the impedance-matching level between the two resonances remains close to -10.3 dB. After adding the cross-shaped perturbation structure in Antenna c, the in-band hump is reduced to approximately -18 dB, and the two resonant modes are more smoothly connected over 26.35–29.20 GHz. These numerical results confirm that the wideband response is produced by the coupling and merging of the adjacent electric- and magnetic-dipole modes rather than by a single aperture resonance.

3. SIMULATION RESULTS AND ANALYSIS

Figure 7 shows the simulated reflection coefficient of the proposed antenna. It can be observed that the antenna satisfies $|S_{11}| < -10$ dB over the frequency range of 26.35–29.20 GHz, with a center frequency of approximately 27.78 GHz and a fractional impedance bandwidth of approximately 10.26%. Two distinct resonant points can be identified within the operating band, located at approximately 27.3 and 28.58 GHz, where the lower resonance is mainly attributed to the magnetic-dipole mode excited by the SIW slot coupling, central coupling patch, and metallized vias, whereas the higher resonance originates primarily from the electric-dipole mode excited by the central cross-shaped perturbation structure and split arc-shaped patches. The effective overlap and merging of these two adjacent resonant modes enable the antenna to achieve good wideband impedance matching across the entire target band. The fractional impedance bandwidth is calculated as follows:

$$\mathrm{FBW} = \frac{f_H - f_L}{f_C} \times 100\% \tag{2}$$

Figure 8 presents the simulated realized-gain radiation patterns of the proposed antenna in the $\varphi = 0^\circ$ and $\varphi = 90^\circ$ planes at 26, 27, 28, and 29 GHz. At all investigated frequencies, the main beam remains approximately oriented toward the boresight direction, demonstrating generally consistent broadside radiation characteristics. Although slight variations in beamwidth and backward radiation are observed near the band edges, no evident main-beam splitting occurs. The peak realized gains at 26, 27, 28, and 29 GHz are approximately

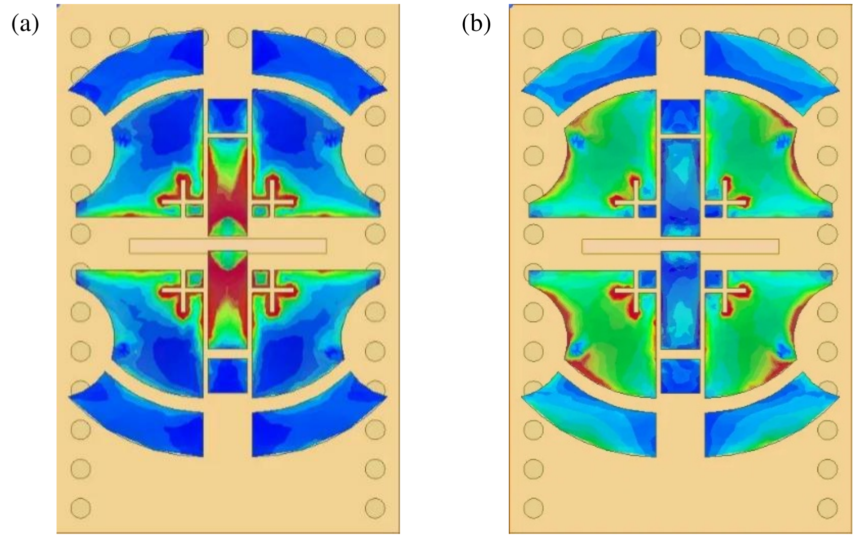

FIGURE 5. Current distributions for the patch at two resonance points. (a) 28.58 GHz. (b) 27.3 GHz.

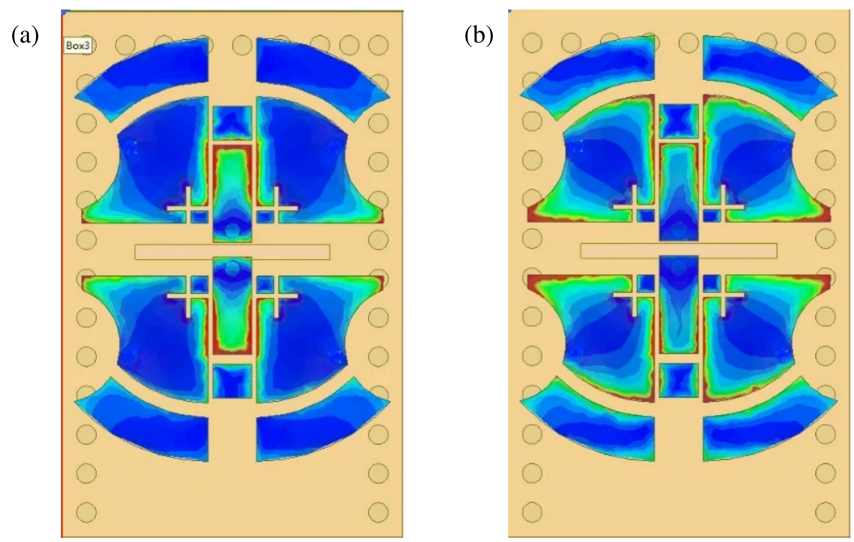

FIGURE 6. Electric-field distributions of the proposed antenna. (a) 28.58 GHz and (b) 27.3 GHz.

6.61, 7.90, 8.15, and 7.89 dBi, respectively. Within the simulated impedance bandwidth, the peak realized gain varies by only approximately 0.26 dB from 27 to 29 GHz, indicating relatively stable in-band gain performance. The lower realized gain at 26 GHz is mainly attributed to the fact that this frequency is slightly below the lower edge of the -10-dB impedance bandwidth.

Figure 9 shows the simulated peak realized gain, radiation efficiency, and total efficiency of the proposed antenna. The radiation efficiencies at 26, 27, 28, and 29 GHz are approximately 99.2%, 99.5%, 99.7%, and 99.5%, respectively. The corresponding total efficiencies are approximately 81.8%, 98.7%, 98.2%, and 95.4%, respectively. The relatively lower total efficiency at 26 GHz is mainly caused by impedance mismatch because this frequency lies slightly outside the simulated -10 dB impedance bandwidth. Within the operating band, the antenna maintains both high radiation efficiency and high total efficiency.

Figure 10 presents the simulated co-polarized and cross-polarized realized-gain patterns at 28 GHz based on the Ludwig-3 polarization definition. The L3X component represents the dominant co-polarization, whereas the L3Y component represents the cross-polarization. In both principal planes, the co-polarized component is dominant within the main-beam region, and the maximum cross-polarization level remains below approximately -18 dBi, indicating good linear-polarization purity.

Since the proposed antenna is linearly polarized rather than circularly polarized, the axial ratio is not considered an applicable performance metric. The multi-frequency patterns show no evident main-beam splitting. Although slight variations in backward radiation and secondary lobes are observed near the band edges, the overall pattern shape remains consistent within the operating band.

To further clarify the influence of key structural parameters on the antenna's impedance-matching characteristics, a

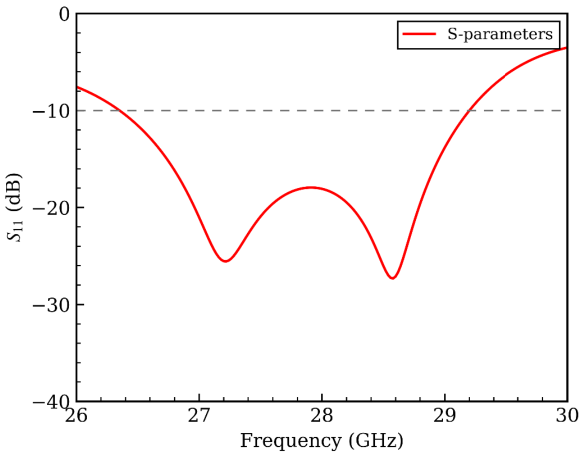

FIGURE 7. Simulated reflection coefficient of the proposed SIW slot antenna.

comparative parametric optimization was conducted with the coupling-slot length L_s, central coupling-patch length L_2, and cross-shaped perturbation length $L_{\rm tt}$. In each case, only a single parameter was varied while the others were kept at their optimal values, and the final optimized structure was adopted as the reference model. By comparing the reflection coefficient under different parameter values, the respective effects of each structural element on the resonant frequency, matching depth, and impedance bandwidth can be identified.

Figure 11 shows the variation of the reflection coefficient with the coupling-slot length L_s. Serving as the energy-coupling channel between the bottom SIW cavity and the upper radiating structure, L_s directly governs the interlayer coupling strength and significantly affects the relative positions of the two resonant modes as well as the in-band matching. When L_s is reduced to 3.8 mm, the interlayer coupling becomes weak, and the spacing between the two resonances increases, raising the return-loss hump between them to about -13 dB and degrading the in-band matching margin and flatness; meanwhile, the higher resonance becomes deep and sharp, indicating a concentrated response that is sensitive to fabrication tolerances. When L_s is increased to 4.2 mm, the coupling is enhanced and tends toward over-coupling, shifting the lower resonance toward lower frequencies and deepening it, while the matching at the higher band becomes shallow and the upper $|S_{11}| < -10$ dB edge frequency moves leftward, resulting in a reduced effective impedance bandwidth. When $L_s = 4.0$ mm, the interlayer coupling strength is moderate, and the lower and higher resonances are well connected within the target band, yielding sufficient in-band matching and the best flatness with an optimal impedance bandwidth. Therefore, $L_s = 4.0$ mm is finally selected.

Figure 12 shows the variation of the reflection coefficient with the central coupling patch length L_2. Located directly above the coupling slot, the central coupling patch dominates the lower resonant mode, and its length directly determines the equivalent current path in the central region, thereby significantly affecting the position of the resonant frequencies. When L_2 is reduced to 1.8 mm, the equivalent current path is shortened, and both resonances shift toward higher frequencies with an increased spacing, raising the return-loss hump between them to about -12 dB, which approaches the -10 dB threshold and markedly degrades the in-band matching. When L_2 is increased to 2.2 mm, the equivalent current path is lengthened and both resonances move toward lower frequencies and become considerably shallower; in particular, the higher resonance reaches only about -17 dB, and the upper $|S_{11}| < -10$ dB edge frequency shifts substantially leftward, causing severe mismatch in the higher band and a sharp reduction of the effective bandwidth. When $L_2 = 2.0$ mm, the two resonances are located at appropriate positions within the target band, with moderate spacing and balanced depths, yielding the most sufficient in-band matching. Therefore, $L_2 = 2.0$ mm is finally selected.

Figure 13 shows the variation of the reflection coefficient with the cross-shaped perturbation length $L_{\rm tt}$. Embedded between the central coupling patch and the split arc-shaped patches, the cross-shaped perturbation structure introduces a capacitive perturbation that tunes the impedance transition between the adjacent resonant modes, primarily affecting the distribution of the matching depth between the two resonances and the in-band flatness, while exerting minimal influence on the resonant-frequency positions. When $L_{\rm tt} = 0.8$ mm, the capacitive perturbation is weak; the lower resonance is deep while the higher resonance is shallow; and the matching depths of the two resonances are unbalanced. When $L_{\rm tt} = 1.0$ mm, the capacitive perturbation is enhanced, and the higher resonance is further deepened, but the upper $|S_{11}| < -10$ dB edge frequency moves leftward, shrinking the higher-frequency coverage. When $L_{\rm tt} = 0.9$ mm, the impedance transition between adjacent modes is optimal; the matching depths of the lower and higher resonances become balanced; the in-band flatness is the best; and the edge frequencies at both ends of the operating band are symmetric. Therefore, $L_{\rm tt} = 0.9$ mm was selected.

In summary, the three key parameters dominate the antenna's different characteristics: the coupling-slot length L_s controls the interlayer coupling strength and the spacing between the two resonances; the central coupling-patch length L_2 determines the positions of the resonant frequencies; and the cross-shaped perturbation length $L_{\rm tt}$ tunes the in-band matching depth and flatness. Their joint optimization enables the antenna to achieve sufficient and stable wideband impedance matching in the target band.

4. MEASUREMENT AND ERROR ANALYSIS

To verify the practical performance of the proposed antenna, a prototype was fabricated and tested. The antenna was implemented on dual-layer Rogers RT/Duroid 5880 substrates and formed using a lamination bonding process, with the fabricated prototype shown in Fig. 14. To reduce the assembly errors caused by manual alignment, a lamination bonding process was adopted instead of conventional manual alignment with auxiliary holes, thereby effectively reducing additional losses and fabrication tolerances.

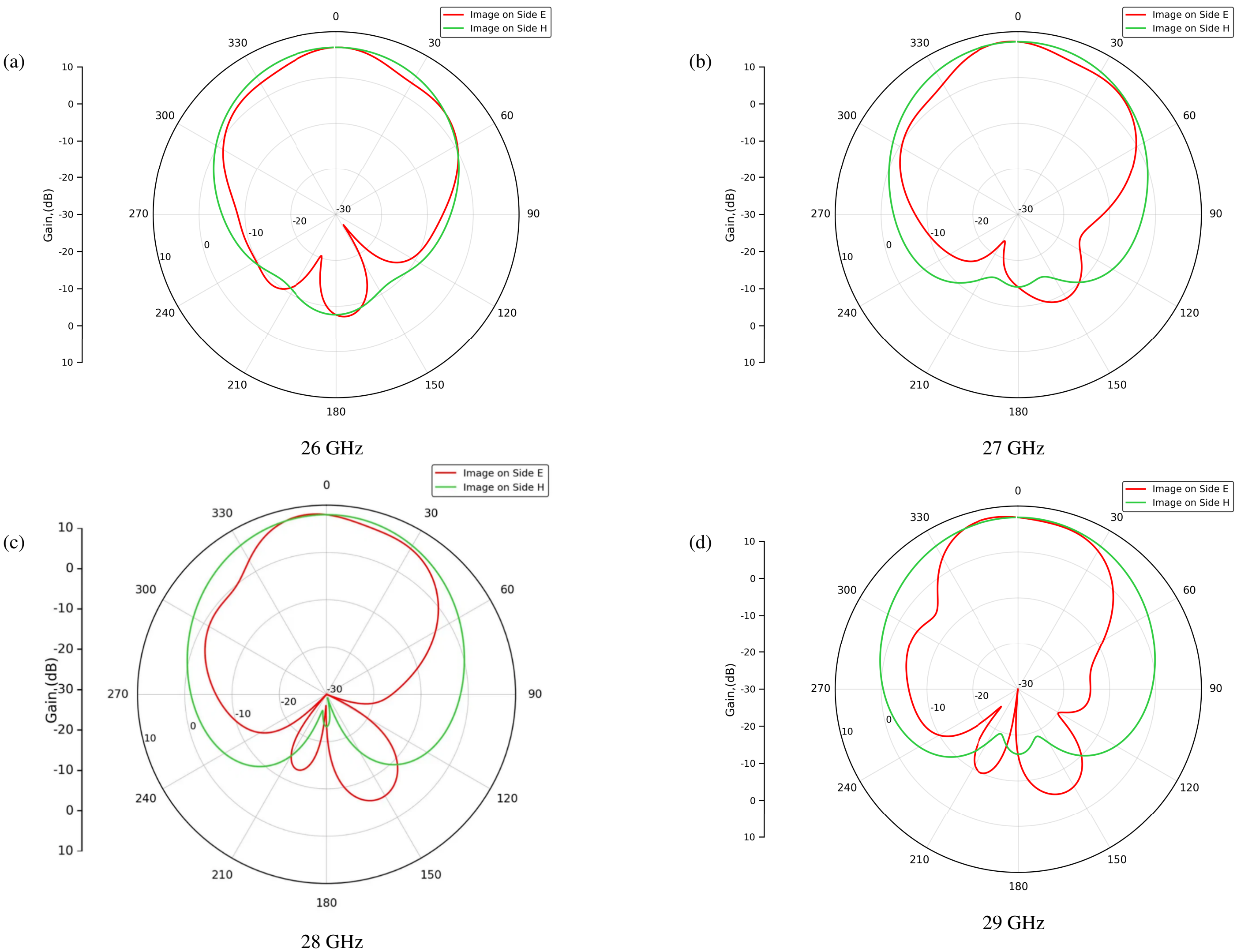

FIGURE 8. Simulated realized-gain radiation patterns of the proposed antenna in the $\varphi = 0^\circ$ and $\varphi = 90^\circ$ planes at: (a) 26 GHz, (b) 27 GHz, (c) 28 GHz, and (d) 29 GHz.

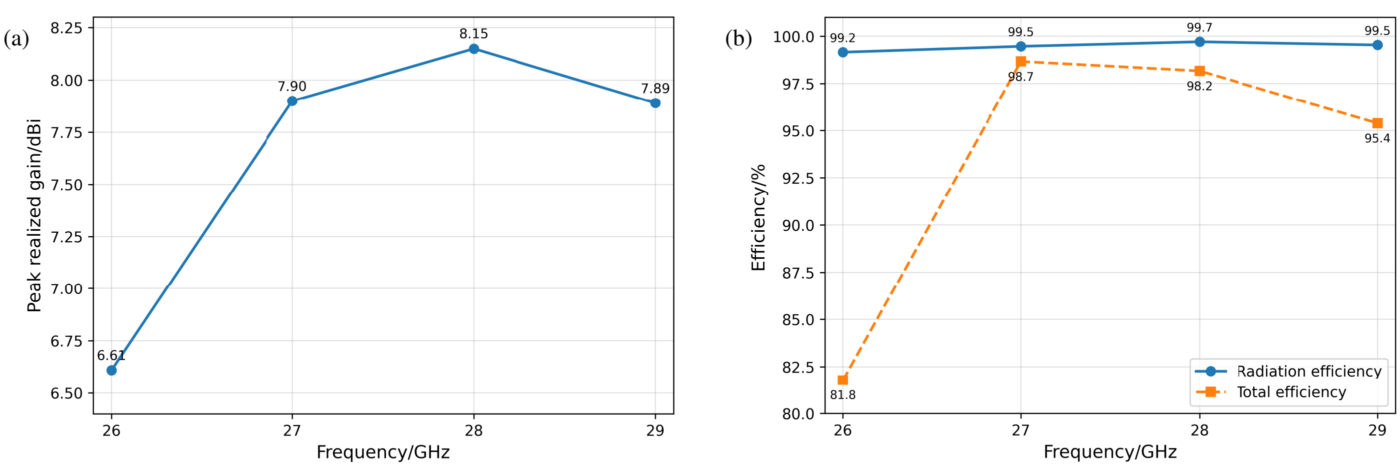

FIGURE 9. Simulated radiation performance of the proposed antenna: (a) peak realized gain and (b) radiation and total efficiencies.

The reflection coefficient of the fabricated antenna was measured using a vector network analyzer covering the Ka-band frequency range. The measurement system was calibrated before the test. During the measurement, the prototype and test cable were carefully fixed to reduce fluctuations caused by cable movement and unstable electrical contact. The reflection

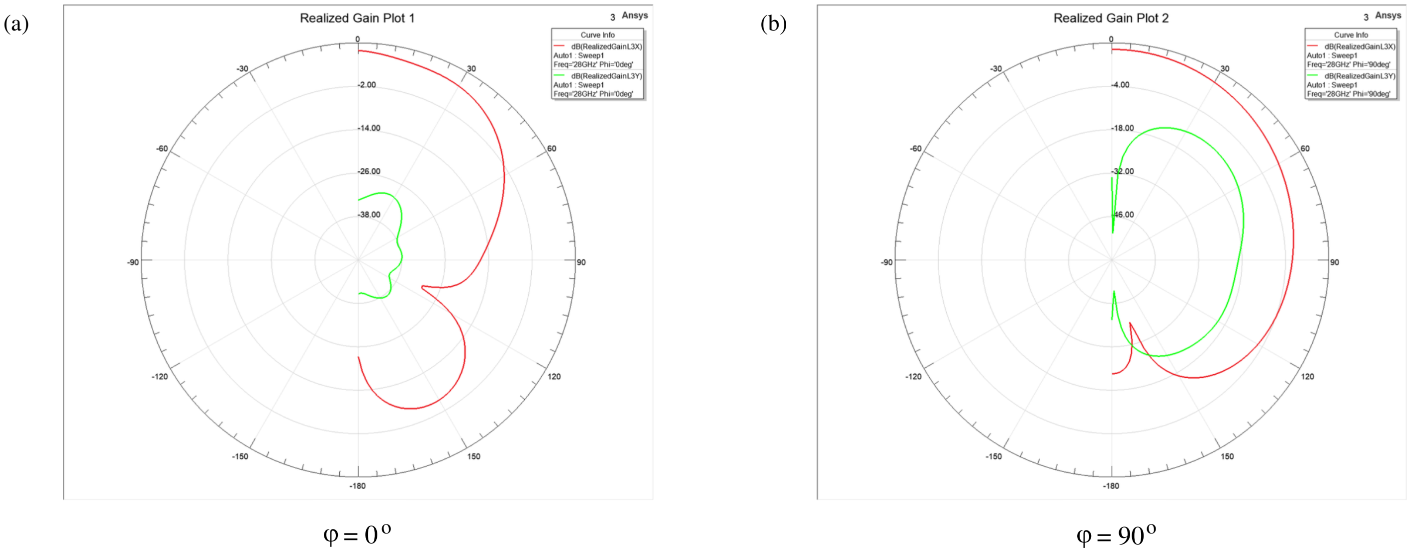

FIGURE 10. Simulated co-polarized and cross-polarized realized-gain patterns of the proposed antenna at 28 GHz in the: (a) $\varphi = 0°$ and (b) $\varphi = 90°$ planes.

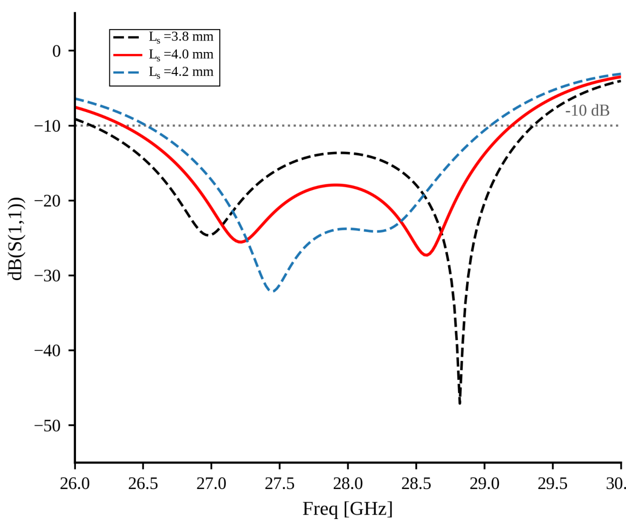

FIGURE 11. Simulated reflection coefficients under different coupling slot lengths L_s.

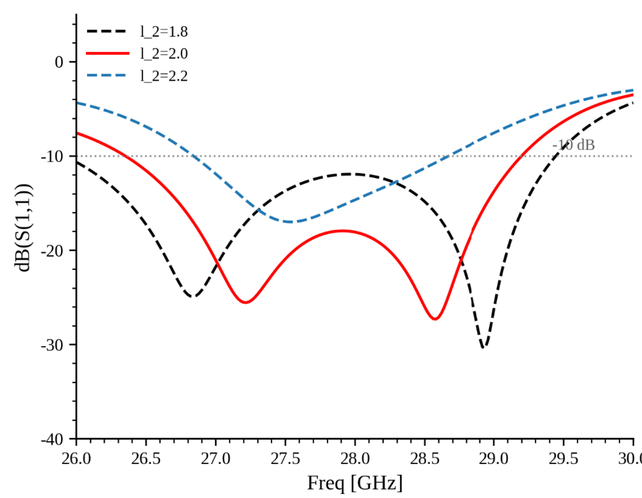

FIGURE 12. Simulated reflection coefficients under different values of L_2.

coefficient was recorded over 26–30 GHz and subsequently compared with the simulated result.

Figure 15 compares the antenna's measured and simulated reflection coefficients. The measured curve generally follows the trend of simulated curve, and both exhibit a distinct dual-resonance wideband characteristic within the operating band. The measured results indicate that the antenna satisfies $|S_{11}| < -10$ dB over approximately 26.8–29.1 GHz, corresponding to a fractional bandwidth of approximately 8.2%, which is in good agreement with the simulated range of 26.35–29.20 GHz, supporting the impedance-matching effectiveness and fabrication feasibility of the proposed split magnetic-electric dipole structure with multi-mode coupling. The measured curve was slightly shallower than the simulated one, with the band edges at both ends slightly inward. These deviations are mainly caused by fabrication and measurement errors. The dual-layer laminated substrate structure may introduce interlayer misalignment and small air gaps during bonding, altering the coupling strength between the upper and lower layers and thus slightly changing the resonance depths and band-edge matching. In addition, tolerances in substrate thickness, drift in relative permittivity at millimeter-wave frequencies, and fabrication errors in metallized vias can disrupt structural symmetry and impedance continuity, affecting matching at certain frequency points. Moreover, the residual calibration errors of the vector network analyzer, test-cable losses, and environmental electromagnetic interference also introduce additional fluctuations into the measured curve. Despite these deviations, the measured and simulated results show reasonably consistent resonance positions and similar overall trends, demonstrating the sound rationality and engineering feasibility of the proposed antenna structure. It should be noted that the experimental valida-

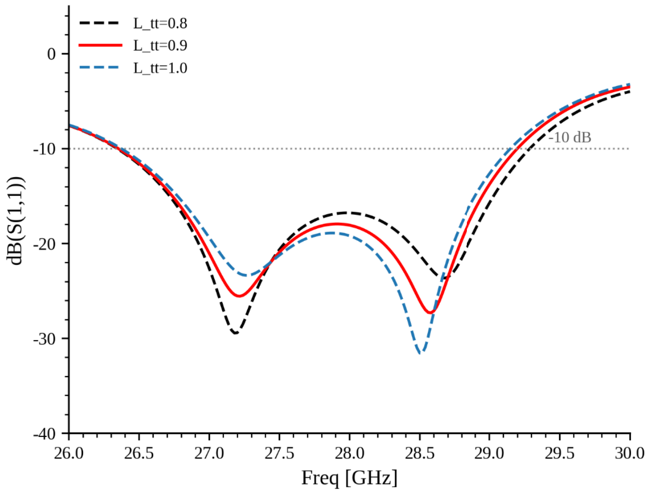

FIGURE 13. Simulated reflection coefficients under different values of L_{tt}.

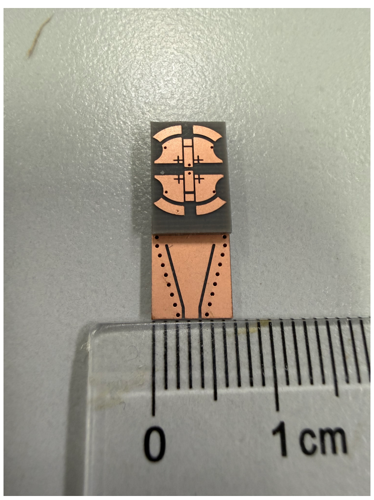

FIGURE 14. Fabricated prototype of the proposed SIW slot antenna.

tion in this work is limited to the reflection-coefficient measurement. Due to current limitation of the available Ka-band far-field measurement conditions, fully calibrated measurements of the radiation patterns, realized gain, and radiation efficiency cannot be provided at this stage. Therefore, the radiation characteristics reported in this work are evaluated using full-wave electromagnetic simulations, and the measured results are used to verify impedance-matching performance and practical feasibility of the fabricated antenna.

Table 2 compares the proposed antenna with recently reported Ka-band SIW and magnetic-electric dipole antennas. The array-based designs generally provide wider bandwidths and higher gains because of their larger effective apertures, multiple radiating elements, and corporate-feed networks. However, these advantages are accompanied by increased footprint, layer count, and feeding complexity. In contrast, the proposed antenna employs a compact two-layer single-element configuration without an array feeding network or an additional superstrate. Although its realized gain is lower than those of array-based designs, it provides a favorable compromise

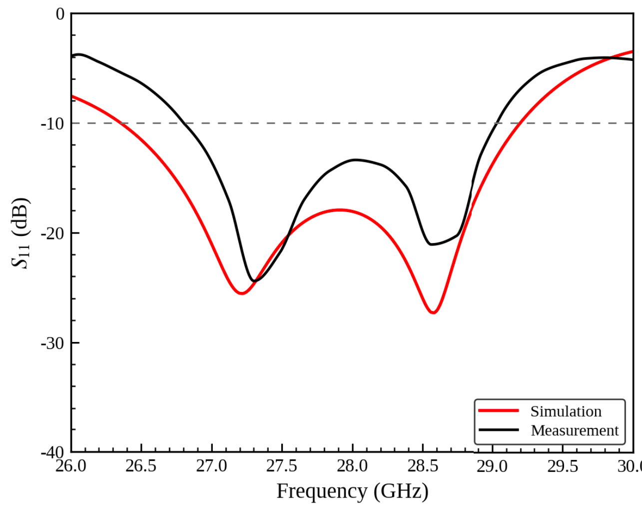

FIGURE 15. Simulated and measured reflection coefficients of the proposed SIW slot antenna.

TABLE 2. Comparison with recently reported Ka-band SIW and magnetic-electric dipole antennas.

Ref.	Freq. band (GHz)	FBW (%)	Gain
[19]	29.28–35.83	21.80	14.1 (dBic)
[22]	24.12–30.83	24.42	11.02 (dBi)
[25]	27.58–32.71	17.02	11.5 (dBi)
[28]	25.00–30.00	18.18	8.50 (dBi)
This work	26.35–29.20	10.26	8.15 (dBi)

among continuous impedance bandwidth, realized gain, simulated efficiency, electrical size, structural complexity, and planar integration.

5. CONCLUSION

In this study, a wideband substrate-integrated waveguide (SIW) slot antenna based on a split magnetic-electric dipole with multi-mode coupling is proposed and implemented. The antenna adopts a dual-layer dielectric substrate configuration, in which the bottom layer serves as the SIW feeding layer that achieves low-loss energy transmission and interlayer coupling through periodic metallized vias and a coupling slot, and the top layer constitutes the split magnetic-electric dipole radiating layer, where split arc-shaped patches, a central coupling patch, a cross-shaped perturbation structure, and metallized vias are introduced to reconstruct the surface current path and excite multiple adjacent resonant modes. The structural evolution and field-distribution analyses demonstrate that the wideband performance of the proposed antenna originates from the synergistic coupling between the electric- and magnetic-dipole modes: the split arc-shaped patches provide the fundamental electric-dipole radiating mode; the central coupling patch and metallized vias introduce a magnetic-dipole component and substantially broaden the bandwidth; and the cross-shaped perturbation structure further deepens the matching depth and improves the in-band flatness, jointly enabling the low- and high-frequency resonant modes to merge within the target band. The simulated results show that the proposed antenna achieves an impedance bandwidth of 26.35–29.20 GHz for $|S_{11}| < -10$ dB and a peak realized gain of 8.15 dBi at 28 GHz. The fabricated prototype achieves a measured impedance bandwidth of approximately 26.8–29.1 GHz, confirming the impedance-matching performance and practical feasibility of the proposed structure. Furthermore, the simulated multi-frequency radiation patterns and efficiency results demonstrate that the antenna maintains high radiation efficiency, stable in-band realized gain, and generally consistent broadside radiation characteristics over the investigated frequency range.

ACKNOWLEDGEMENT

This work was supported by the University-Local Government Scientific and Technical Cooperation Cultivation Project of the Ordos Institute-LNTTU under Grant YJY-XD-2024-B-009.

REFERENCES

[1] Cheng, Y. J., *Substrate Integrated Antennas and Arrays*, CRC Press, 2018.

[2] Chen, Z. N. and X. Qing, *Substrate-Integrated Millimeter-Wave Antennas for Next-Generation Communication and Radar Systems*, John Wiley & Sons, 2021.

[3] Xu, F. and K. Wu, "Guided-wave and leakage characteristics of substrate integrated waveguide," *IEEE Transactions on Microwave Theory and Techniques*, Vol. 53, No. 1, 66–73, 2005.

[4] Hong, W., K. Wu, H. Tang, J. Chen, P. Chen, Y. Cheng, and J. Xu, "Siw-like guided wave structures and applications," *IEICE transactions on electronics*, Vol. 92, No. 9, 1111–1123, 2009.

[5] Luo, G. Q., Z. F. Hu, L. X. Dong, and L. L. Sun, "Planar slot antenna backed by substrate integrated waveguide cavity," *IEEE Antennas and Wireless Propagation Letters*, Vol. 7, 236–239, 2008.

[6] Luo, G. Q., Z. F. Hu, W. J. Li, X. H. Zhang, L. L. Sun, and J. F. Zheng, "Bandwidth-enhanced low-profile cavity-backed slot antenna by using hybrid siw cavity modes," *IEEE Transactions on Antennas and Propagation*, Vol. 60, No. 4, 1698–1704, 2012.

[7] Kang, H. and S. Lim, "Enhanced-gain planar substrate-integrated waveguide cavity-backed slot antenna with rectangular slot window on superstrate," *ETRI Journal*, Vol. 36, No. 6, 1062–1065, 2014.

[8] Saghati, A. P., A. P. Saghati, and K. Entesari, "An ultra-miniature SIW cavity-backed slot antenna," *IEEE Antennas and Wireless Propagation Letters*, Vol. 16, 313–316, 2017.

[9] El Gharbi, M., N. Aknin, and S. Ahyoud, "Design of SIW cavity backed triangular slot antenna using two different feeding transitions," *Procedia Manufacturing*, Vol. 32, 687–693, 2019.

[10] Nayak, A. K., I. M. Filanovsky, K. Moez, and A. Patnaik, "A dual-band multilayer SIW cavity backed differential slot antenna," in *2022 IEEE International Symposium on Antennas and Propagation and USNC-URSI Radio Science Meeting (AP-S/URSI)*, 2022–2023, Denver, CO, USA, 2022.

[11] Kumar, A. and S. Raghavan, "Wideband slotted substrate integrated waveguide cavity-backed antenna for Ku-band application," *Microwave and Optical Technology Letters*, Vol. 59, No. 7, 1613–1619, 2017.

[12] Niu, B. and J.-H. Tan, "Bandwidth enhancement of low-profile SIW cavity antenna with bilateral slots," *Progress In Electromagnetics Research Letters*, Vol. 82, 25–32, 2019.

[13] Kumar, A., M. Kumar, and A. K. Singh, "Substrate integrated waveguide cavity backed wideband slot antenna for 5G applications," *Radioengineering*, Vol. 30, No. 3, 480–487, 2021.

[14] Tong, X., Z. H. Jiang, C. Yu, F. Wu, X. Xu, and W. Hong, "Low-profile, broadband, dual-linearly polarized, and wide-angle millimeter-wave antenna arrays for ka-band 5g applications," *IEEE Antennas and Wireless Propagation Letters*, Vol. 20, No. 10, 2038–2042, 2021.

[15] Park, S.-J., D.-H. Shin, and S.-O. Park, "Low side-lobe substrate-integrated-waveguide antenna array using broadband unequal feeding network for millimeter-wave handset device," *IEEE Transactions on Antennas and Propagation*, Vol. 64, No. 3, 923–932, 2016.

[16] Li, X., J. Xiao, Z. Qi, and H. Zhu, "Broadband and high-gain SIW-fed antenna array for 5G applications," *IEEE Access*, Vol. 6, 56 282–56 289, 2018.

[17] Karami, F., P. Rezaei, A. Amn-e Elahi, A. Abolfathi, and A. A. Kishk, "Broadband and efficient patch array antenna fed by substrate integrated waveguide feed network for ku-band satellite applications," *International Journal of RF and Microwave Computer-Aided Engineering*, Vol. 31, No. 9, e22772, 2021.

[18] Wang, J., Y. Li, J. Wang, L. Ge, M. Chen, Z. Zhang, and Z. Li, "A low-profile vertically polarized magneto-electric monopole antenna with a 60for millimeter-wave applications," *IEEE Transactions on Antennas and Propagation*, Vol. 69, No. 1, 3–13, 2021.

[19] Xu, J., Y. Xie, and J. Zhao, "Siw broadband circularly polarized high-gain low-profile magneto-electric dipole antenna array," *Microwave and Optical Technology Letters*, Vol. 66, No. 11, e70033, 2024.

[20] Bozzi, M., A. Georgiadis, and K. Wu, "Review of substrate-integrated waveguide circuits and antennas," *IET Microwaves, Antennas & Propagation*, Vol. 5, No. 8, 909–920, 2011.

[21] Mukherjee, S., A. Biswas, and K. V. Srivastava, "Broadband substrate integrated waveguide cavity-backed bow-tie slot antenna," *IEEE Antennas and Wireless Propagation Letters*, Vol. 13, 1152–1155, 2014.

[22] Gao, M., R. Huang, X. Du, and B. Tao, "Design of a three-layer SIW broadband 1×4 dipole patch array antenna driven by slot feeding," *Progress In Electromagnetics Research C*, Vol. 168, 138–148, 2026.

[23] Aparna, E., G. Ram, and G. A. Kumar, "Review on substrate integrated waveguide cavity backed slot antennas," *IEEE Access*, Vol. 10, 133 504–133 525, 2022.

[24] De, R., M. P. Abegaonkar, and A. Basu, "Compact dual slot SIW cavity backed antenna for CubeSat/nanosatellite applications," *IEEE Access*, Vol. 11, 78 802–78 810, 2023.

[25] Ma, Z., Z. Wang, and Z. Duan, "Broadband SIW cavity-backed novel slot antenna with a shorting-via for ka-band applications," *IEEE Access*, Vol. 12, 174 705–174 712, 2024.

[26] Oh, S. U., H. Yoo, and T. H. Jang, "A low-profile millimeter-wave broadband magneto electric dipole antenna with fragmented dipole arm," *IEEE Transactions on Antennas and Propagation*, Vol. 73, No. 2, 1203–1208, Feb. 2025.

[27] Sarani, V., E. M. Ali, M. Shariatifar, B. S. Virdee, D. Mariyanayagam, N. Rashid, M. Alibakhshikenari, and M. Dalarsson, "Wideband circularly-polarized hexagonal SIW cavity-backed slot antenna with enhanced bandwidth and compact design," *IEEE Access*, Vol. 13, 80 407–80 415, 2025.

[28] Askari, H., N. Hussain, M. A. Sufian, S. M. Lee, and N. Kim, "A wideband circularly polarized magnetoelectric dipole antenna for 5G millimeter-wave communications," *Sensors*, Vol. 22, No. 6, 2338, 2022.